# Coupled backward- and forward-propagating solitons in a composite right- and left-handed transmission line

G. P. Veldes,[1,2] J. Cuevas,[3] P. G. Kevrekidis,[4] and D. J. Frantzeskakis[1]

[1]*Department of Physics, University of Athens, Panepistimiopolis, Zografos, Athens 15784, Greece*

[2]*Department of Electronics, Technological Educational Institute of Lamia, Lamia 35100,Greece*

[3]*Grupo de Física No Lineal, Universidad de Sevilla. Departamento de Física Aplicada I, Escuela Politécnica Superior, C/ Virgen de África, 7, 41011 Sevilla, Spain*

[4]*Department of Mathematics and Statistics, University of Massachusetts, Amherst Massachusetts 01003-4515, USA*

We study the coupling between backward- and forward-propagating wave modes, with the same group velocity, in a composite right- and left-handed nonlinear transmission line. Using an asymptotic multiscale expansion technique, we derive a system of two coupled nonlinear Schrödinger equations governing the evolution of the envelopes of these modes. We show that this system supports a variety of backward- and forward-propagating vector solitons of the bright-bright, bright-dark, and dark-bright type. Performing systematic numerical simulations in the framework of the original lattice that models the transmission line, we study the propagation properties of the derived vector soliton solutions. We show that all types of the predicted solitons exist, but differ on their robustness: Only bright-bright solitons propagate undistorted for long times, while the other types are less robust, featuring shorter lifetimes. In all cases, our analytical predictions are in very good agreement with the results of the simulations, at least up to times of the order of the solitons' lifetimes.

PACS number(s): 41.20.Jb, 42.65.Tg, 78.20.Ci

## I. INTRODUCTION

Left-handed (LH) metamaterials are artificial, effectively homogeneous structures, featuring negative refractive index at specific frequency bands where the effective permittivity $\epsilon$ and permeability $\mu$ are simultaneously negative [1–3]. In fact, all known realizations of LH metamaterials rely on the use of common right-handed (RH) elements and thus in a realistic situation such a composite material features both LH and RH behavior in certain frequency bands. Physically speaking, the difference between the two is that in the LH (RH) regime, the energy and the wave fronts of the electromagnetic (em) waves propagate in the opposite (same) directions, giving rise to backward- (forward-) propagating waves.

Transmission line (TL) theory constitutes a convenient framework for the analysis of LH metamaterials. Such an analysis relies on the connection of the em properties of the medium ($\epsilon$ and $\mu$) with the electric elements of the TL's unit cell, namely, the serial and shunt impedance. As mentioned above, in practice, composite right- and left-handed (CRLH) structures are quite relevant, giving rise to pertinent CRLH-TL models. These models are in fact dynamical lattices that can be used for the description of a variety of metamaterial-based devices and systems, such as resonators, directional couplers, and antennas [1–4].

Nonlinear CRLH-TL models, with a serial and/or shunt impedance depending on voltages or currents, have also attracted attention. Such structures may be realized by inserting diodes, which mimic voltage-controlled nonlinear capacitors, into resonant conductive elements (such as split-ring resonators) [5–7]. Such nonlinear CRLH-TL models have been used in various works dealing, e.g., with the parametric shielding of em fields [8], the long-wave–short-wave interaction [9], or soliton formation [10–12]. Experiments in nonlinear CRLH-TL models have also been performed (see [13]) and

the formation of bright [14,15] and dark [15,16] envelope solitons, described by an effective nonlinear Schrödinger (NLS) equation, was reported. Notice that in earlier studies on RH-TL models it was shown that two (or more) solitons propagating with the same group velocity can be described by a system of two (or more) NLS equations [17] (see also [18] for theoretical as well as experimental results). Such coupled NLS equations have been studied extensively in nonlinear optics and mathematical physics; see, e.g., Refs. [19–21] and references therein. They are well known to give rise to a variety of vector solitons, including bright-bright (BB), bright-dark (BD), and dark-dark (DD) ones.

In this work we study analytically and numerically the interaction between backward- and forward-propagating solitons in a nonlinear CRLH-TL model. Our model is a nonlinear version of a generic CRLH-TL model, particularly relevant to the context of LH metamaterials (see, e.g., Refs. [2,4]). The considered nonlinear element in the unit cell of the TL is the shunt capacitor, which simulates the presence of a heterostructure barrier varactor (HBV) diode [6] (the capacitance of the HBV diode depends on the applied voltage). Starting from the discrete lump element model of the CRLH TL, we derive a nonlinear lattice equation. First, we study the linear regime and show that for certain frequency bands, RH and LH modes can propagate with the same group velocity. Then we treat the nonlinear lattice equation in the framework of the quasidiscrete (or quasicontinuum) approximation (see, e.g., [15,19,22,23] for a review): we thus seek envelope soliton solutions of the nonlinear lattice model, characterized by a discrete carrier and a continuum envelope and employ an asymptotic multiscale expansion method to derive a system of two coupled NLS equations. Each of these equations describes the evolution of the envelope of a backward- (LH) and a forward-propagating (RH) mode.

A systematic analysis of the system of the NLS equations reveals the existence, in certain frequency bands, of three different types of vector solitons: (a) a backward-propagating bright soliton coupled with a forward-propagating bright soliton, (b) a backward-propagating bright soliton coupled with a forward-propagating dark soliton, and (c) a backward-propagating dark soliton coupled with a forward-propagating bright soliton. This way we propose and study in detail all possible vector solitons in this nonlinear CRLH-TL setting, highlighting how individual soliton components interact via the nonlinearity induced by the insertion of the HBV diodes. Importantly, our analysis suggests how the characteristics (amplitude, width, etc.) of each solitonic mode can control the ones of the other mode; this possibility arises from the fact that the relevant parameters of each soliton are connected with the ones of the other soliton, thus providing a means to adjust, e.g., the amplitude or width of the LH mode by changing the parameters of the RH mode.

The above analytical predictions are then tested against direct numerical simulations, which are performed in the framework of the original nonlinear lattice model. The results of the simulations verify the existence of the aforementioned types of vector solitons in the full TL model, but also offer important information regarding their robustness. In particular, the results of direct simulations performed for long times indicate that BB solitons are the most robust among the members of the vector soliton family. Indeed, the mixed [dark-bright (DB) or BD] types are found to be less robust; however, the DB solitons in a specific frequency band, although deformed during their evolution, are found to be more robust than those in other bands, as well as the bright-dark solitons, which are destroyed for the same propagation time. The observed long-time behavior of the above solitons of the mixed type may be qualitatively explained, in the framework of the effective coupled NLS description, by the following fact: in the less robust cases, the continuous-wave background carrying the dark soliton is prone to modulational instability [18,24], while in the more robust case it is not. In any case, our results indicate the existence of all three types: robustness of BB solitons and partial or substantial deformation of the other types. We can thus conclude that bright-bright (LH-RH) solitons, as well as dark-bright (LH-RH) solitons in certain frequency bands, have a better chance of being observed in experiments.

The paper is organized as follows. In Sec. II we introduce the nonlinear CRLH-TL model and the pertinent lattice equation and derive the system of the two coupled NLS equations (relevant details are also appended in the Appendices). In Sec. III we present analytical and numerical results for each type of vector soliton. Finally, in Sec. IV we summarize and give our conclusions.

## II. THE MODEL AND ITS ANALYTICAL CONSIDERATIONS

### A. The nonlinear CRLH-TL model

We consider a generic CRLH-TL model, composed by both right- and left-handed elements, as shown in its unit-cell circuit in Fig. 1 [2,4]. The (RH) elements of this TL are the inductance
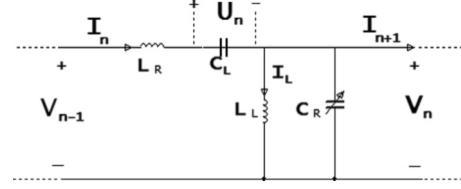


FIG. 1. Unit-cell circuit of the nonlinear CRLH model.

$L_R$ and capacitance $C_R$, while the LH ones are the inductance $L_L$ and capacitance $C_L$. We assume that the TL is loaded with a nonlinear capacitance ($C_R$, while the capacitance $C_L$ will be assumed to be fixed and voltage independent). This can be implemented by proper insertion of diodes in the TL (see, e.g., pertinent experiments as well as theoretical work in Refs. [10–16]); in other words, we assume that the shunt capacitor $C_R$ is nonlinear (see details below).

Let us now consider Kirchhoff's voltage and current laws for the unit-cell circuit of Fig. 1, which respectively read

$$V_{n-1} = V_n + L_R \frac{dI_n}{dt} + U_n, \qquad (1)$$

$$I_n = I_{n+1} + I_L + \frac{d}{dt}(C_R V_n), \qquad (2)$$

where $U_n$ is the voltage across the capacitance $C_L$ and $I_L$ is the current across the inductor $L_L$. The above equations, together with the auxiliary equations $V_n = L_L dI_L/dt$ and $I_n = C_L dU_n/dt$, lead to the following system:

$$L_R L_L C_L \frac{d^4}{dt^4}(C_R V_n) + L_L \frac{d^2}{dt^2}(C_R V_n) + L_R C_L \frac{d^2 V_n}{dt^2}$$
$$- L_L C_L \frac{d^2}{dt^2}(V_{n+1} + V_{n-1} - 2V_n) + V_n = 0. \qquad (3)$$

To proceed further, we now consider a specific voltage dependence for the nonlinear capacitance $C_R$. Here we will assume that for sufficiently small values of the voltage $V_n$, the function $C_R(V_n)$ can be approximated as follows, via a Taylor expansion:

$$C_R(V_n) \approx C_{R0} + C'_{R0}(V_n - V_0) + \tfrac{1}{2}C''_{R0}(V_n - V_0)^2, \quad (4)$$

where $C_{R0} \equiv C_R(V_0)$ is a constant capacitance corresponding to the bias voltage $V_0$, while $C'_{R0}$ and $C''_{R0}$ also assume constant values, depending on the particular form of $C_R(V)$. Below we will further discuss this approximation, in connection with the HBV diode, used in the experiments described in Ref. [13] (similar varactor-type diodes were also used in the experiments of Ref. [7]).

Next, substituting Eq. (4) into Eq. (3) and using the scale transformations $t \to \omega_{sh} t$ [where $\omega_{sh}^2 = (L_L C_{R0})^{-1}$] and $V_n \to [C'_{R0}(2C_{R0})^{-1}]V_n$, we obtain

$$\frac{d^4 V_n}{dt^4} - \beta^2 \frac{d^2}{dt^2}(V_{n+1} + V_{n-1} - 2V_n) + (1 + \delta^2)\frac{d^2 V_n}{dt^2}$$
$$+ \delta^2 V_n + \delta^2 \frac{d^2 V_n^2}{dt^2} + \delta^2 \mu \frac{d^2 V_n^3}{dt^2} + \frac{d^4 V_n^2}{dt^4} + \mu \frac{d^4 V_n^3}{dt^4} = 0,$$
$$(5)$$

where the constant parameters $\delta$, $\beta$, and $\mu$ are given by

$$\delta = \frac{f_{se}}{f_{sh}}, \quad \beta = \frac{f_{RH}}{f_{sh}}, \quad \mu = \frac{2C''_{R0}}{3C'^2_{R0}}C_{R0}. \qquad (6)$$

In the above expressions, $f_{se}$ and $f_{sh}$ denote series and shunt frequencies, respectively, and $f_{RH}$ denotes the characteristic frequency related to the RH part of the unit-cell circuit; the above frequencies are defined as

$$f_{se} = \frac{1}{2\pi\sqrt{L_R C_L}}, \quad f_{sh} = \frac{1}{2\pi\sqrt{L_L C_{R0}}},$$

$$f_{RH} = \frac{1}{2\pi\sqrt{L_R C_{R0}}}. \tag{7}$$

Note that if $f_{se}/f_{sh} = 1$, i.e., $\delta = 1$, then the CRLH-TL model is usually referred to as balanced, in the sense that the characteristic impedances of the purely LH and RH TLs, defined as $Z_L = \sqrt{L_L/C_L}$ and $Z_R = \sqrt{L_R/C_{R0}}$, are equal, i.e., $Z_L = Z_R$ [2]. In contrast, if $f_{se}/f_{sh} > 1$, i.e., $\delta > 1$, the LH part of the TL dominates, in the sense that the TL has a more pronounced LH behavior (the serial branch features a capacitive character, while the shunt branch an inductive one). In the opposite case, $f_{se}/f_{sh} < 1$, i.e., $\delta < 1$, the RH part of the TL dominates and the TL has a more pronounced RH behavior (the serial branch features an inductive character, while the shunt branch shows a capacitive one).

It is now relevant to adopt physically relevant parameter values for Eq. (5). For applications in the microwave frequency range (e.g., for microstrip lines [2] or coplanar waveguide structures loaded with split-ring resonators [3]; see also Ref. [23] for recent work), typical values of the capacitances and inductances involved in the CRLH structure are of the order of pF and nH, respectively. Here we will use the values $L_R = 1$ nH, $C_L = 0.1$ pF, and $L_L = 0.12$ nH; thus the frequencies in Eqs. (7) take the values $f_{se} = 15.92$ GHz, $f_{sh} = 14.53$ GHz, and $f_{RH} = 5.03$ GHz. In contrast, as concerns the parameters involved with the nonlinear capacitor $C_R$, we assume that the pertinent capacitance corresponds to a HBV diode, which is characterized by the following equation [6] [see also [7], where the same form of $C(V)$ is used, but different parameter values]:

$$C(V) = C_{j0} A_{da} \left(1 + \frac{|V|}{V_{br}}\right)^{-m}, \tag{8}$$

where $C_{j0} = 1.53$ fF/$\mu$m$^2$ is the capacitance corresponding to bias voltage $V_0 = 0.2$ V, $A_{da} = 650$ $\mu$m$^2$ is the device area, $V_{br} = 12$ V is the breakdown potential, and the exponent $m = 2.7$ results from fitting experimental data. It is clear that, for sufficiently small $V$, by Taylor expanding Eq. (8) one obtains Eq. (4), where the constant parameter values involved are $C_{R0} = 1$ pF, $C'_{R0} = -0.24$ pF/V, and $C''_{R0} = -0.08$ pF/V$^2$. To this end, the values of the normalized parameters $\delta$, $\beta$, and $\mu$ appearing in Eq. (5) take the following values:

$$\delta \approx 1.1, \quad \beta \approx 0.35, \quad \mu \approx -0.9. \tag{9}$$

Below we will use these values for the purposes of our analytical and numerical considerations (we have checked that other values lead to qualitatively similar results). Notice that our choice leads to $\delta > 1$, i.e., we consider the case where the TL has a more pronounced LH character; however, when considering the linear setting (see next section), this parameter will also assume other values, corresponding to the balanced and RH-dominated behavior as well.

## B. Linear analysis

We now assume plane wave solutions of Eq. (5) of the form $V_n = V_0 \exp[i(kn - \omega t)]$, where $k$ and $\omega$ denote the wave number and angular frequency, respectively, and the amplitude of the wave is $V_0 \ll 1$. Substituting the above ansatz into Eq. (5) and keeping only the linear terms in $V_0$, we obtain the following linear dispersion relation:

$$\omega^4 - \left(1 + \delta^2 + 4\beta^2 \sin^2 \frac{k}{2}\right)\omega^2 + \delta^2 = 0. \tag{10}$$

The above result is illustrated in Fig. 2, where we plot the frequency $f/f_{sh}$ as a function of the wave number $k$ (in rad/cell) for three different values of $\delta$ (note that here we consider one period of $k$, i.e., $-\pi \leqslant k_j \leqslant \pi$). It is clear that for $\delta = 1.0954$ [Fig. 2(a)] there exist two frequency bands where em wave propagation is possible: the RH band [high-frequency band depicted by the dashed (blue) line] for $1.0954 < f < 1.4535$ and the LH band [low-frequency band depicted by the solid (red) line] for $0.7538 < f < 1$. In the same case
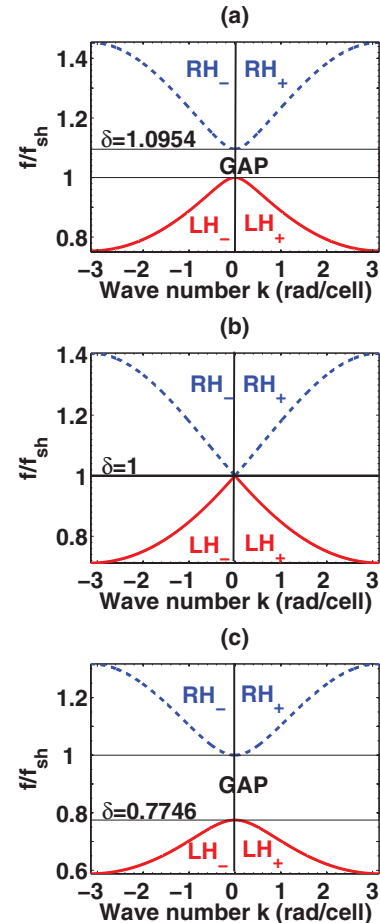


FIG. 2. (Color online) Dispersion relation showing the normalized frequency $f/f_{sh}$ as a function of the wave number $k$ (in rad/cell) for different values of $\delta$: (a) $\delta = 1.0954$, (b) $\delta = 1$, and (c) $\delta = 0.7746$. The solid (red) and dashed (blue) lines show the dispersion relation in the LH low- and RH high-frequency regions, respectively; RH$_\pm$ and LH$_\pm$ denote branches with $k > 0$ or $k < 0$. If $\delta \neq 1$ a gap is formed; the width of the gap is $|\delta - 1|$ for (a) $\delta > 1$ or (c) $\delta < 1$.

($\delta = 1.0954$), there exists a gap for $1 < f/f_{sh} < \delta$ where em wave propagation is not possible.

In the case where $\delta = 1$ (corresponding, e.g., to the value $C_L = 0.12$ pF) the gap vanishes [see Fig. 2(b)] and the TL is balanced. In the balanced case, em wave propagation is possible in two frequency bands as well: the RH band [high-frequency band represented by the dashed (blue) line] with $1 < f/f_{sh} < 1.405$ and the LH band [low-frequency band represented by the solid (red) line] with $0.7117 < f/f_{sh} < 1$.

Finally, for $\delta = 0.7746$ (corresponding, e.g., to $C_L = 0.2$ pF), a gap appears again for $\delta < f/f_{sh} < 1$ [Fig. 2(c)]. In this case too there exist a RH high-frequency band and a LH low-frequency band for $0.588 < f/f_{sh} < 0.7746$ and $1 < f/f_{sh} < 1.317$, respectively. Note that in all cases, the $RH_\pm$ and $LH_\pm$ branches correspond to positive or negative $k$, respectively.

Thus, generally, in the linear setting and for a given frequency the em waves may propagate in either the RH region (forward wave propagation) or the LH region (backward wave propagation). However, in the nonlinear setting, coupling between modes propagating in the LH and RH regimes is possible (see, e.g., relevant earlier work in Refs. [17,18]). Below we will demonstrate that this is the case indeed and study the coupling (interaction) between LH and RH modes with equal group velocities. Since the latter are tangents in the dispersion curves, inspection of Fig. 2 shows that it is possible to identify domains, belonging to the $RH_\pm$ and $LH_\mp$ branches, exhibiting parallel tangents, i.e., equal group velocities.

To further elaborate on this, we may use Eq. (10) to obtain the group velocity $v_g \equiv \partial\omega/\partial k$:

$$v_g = \frac{\omega^3 \beta^2 \sin k}{\omega^4 - \delta^2}. \tag{11}$$

In Fig. 3 we show the dependence of the group velocity $v_g$ on the normalized frequency $f/f_{sh}$ for the values of $\delta$ used in Fig. 2. Notice that the figure depicts only the group-velocity branches with $v_g > 0$ [see solid (red) and dashed (blue) lines] corresponding, respectively, to the $LH_-$ and $RH_+$ branches of the dispersion curves; the branches with $v_g < 0$ (pertinent to the $LH_+$ and $RH_-$ branches of the dispersion curve) are mirror symmetric with respect to the ones shown in the figure, due to the parity of the dispersion relation.

Considering a horizontal cut of the group-velocity curves, say, at $v_g = 0.1$ or $0.075$ [see horizontal lines in Figs. 3(a) and 3(c)], it is readily observed that, indeed, a $LH_-$ and a $RH_+$ mode can share a common group velocity (and interact in the nonlinear regime, as mentioned above). In fact, inspection of the group-velocity curves, say, in Fig. 3(a), shows that the maximum possible common $v_g$ is given by $v_{g_{max}} = 0.1339$, the local maximum of $v_g$, occurring at $f = 0.9391$, in the (shorter in height) LH low-frequency band. Then one can divide each of the LH and RH group-velocity curves into two subregions, depending on the sign of the group-velocity dispersion (GVD) $\partial v_g/\partial \omega$, where such coupling with equal group velocities may occur. These subregions are the subbands I ($0.7538 < f/f_{sh} < 0.9391$) and II ($0.9391 < f/f_{sh} < 1$) for the LH low-frequency band, characterized by positive and negative GVD, respectively, and the subbands III ($1.0954 < f/f_{sh} < 1.1195$) and IV ($1.356 < f/f_{sh} < 1.4535$) for the RH high-frequency band, again characterized by positive and negative GVD,
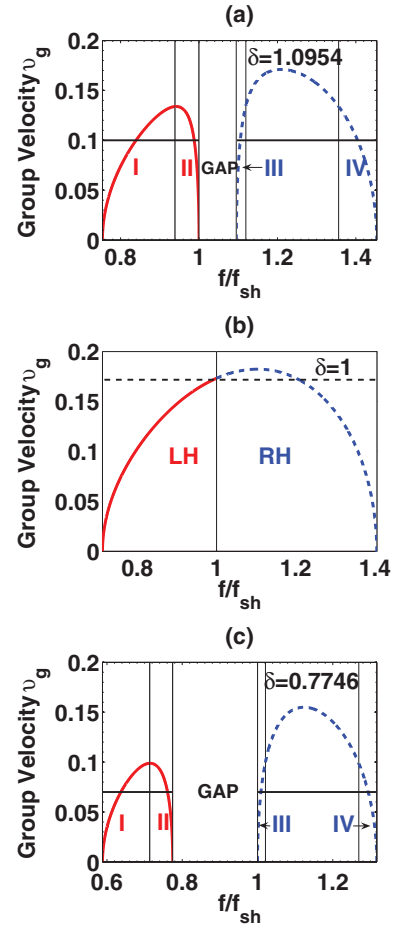
FIG. 3. (Color online) Group velocity $v_g$ as a function of the normalized frequency $f/f_{sh}$ (for the values of $\delta$ used in Fig. 2). The solid (red) and dashed (blue) lines indicate branches corresponding to the $LH_-$ and $RH_+$ regimes, respectively. The intersection of the group velocity curves with the horizontal solid (black) line depicts frequencies of modes with the same group velocity $v_g = 0.1$. Regions I–IV indicate possible interactions between $LH_-$ and $RH_+$ modes with the same $v_g$ but different signs of GVD.

respectively. Thus nonlinear LH and RH modes of equal $v_g$ can feature the following four different possible interactions: (i) the LH mode in band II and RH mode in band IV, both featuring negative GVD; (ii) the LH mode in band I and RH mode in band IV, where the LH (RH) mode features positive (negative) GVD; (iii) the LH mode in band I and RH mode in band III, both featuring positive GVD; and (iv) the LH mode in band II and RH mode in band III, where the LH (RH) mode features negative (positive) GVD.

It is clear that the above set of possibilities arises from the existence of the gap in the considered case with $\delta = 1.0954$. A similar situation also occurs for $\delta < 1$, e.g., for $\delta = 0.7746$, as in Figs. 2(c) and 3(c). In contrast, for $\delta = 1$ the gap no longer exists and thus the only possible interaction is between a LH mode with positive GVD and a RH mode with negative GVD; this interaction can occur for group velocities $v_g \leqslant 0.175$, i.e., beneath the dashed horizontal line in Fig. 3(b). This possibility, however, is already taken into consideration [see case (ii) above]; furthermore, soliton formation in the balanced CRLH-TL model ($\delta = 1$) has already been studied in the literature

[11]. For these reasons, below we will proceed by analyzing the case corresponding to $\delta = 1.0954$, which offers all possible scenarios. It is clear that the case of $\delta = 0.7746$ shares similar qualitative features; this similarity extends beyond the linear wave case and into the nonlinear solitonic one.

Although, as explained above, we are not going to analyze soliton formation and solitons in the special case of the balanced CRLH-TL model with $\delta = 1$, it is worth mentioning that in the case of $\delta = 1$, the dispersion relation exhibits a Dirac point, namely, it is approximately linear in the vicinity of $k = 0$, i.e., $\omega \approx \pm[1 + (\beta/2)k]$ [see Fig. 2(b)]. The emergence of Dirac points is particularly interesting in the two-dimensional (2D) setting of triangular and hexagonal lattices arising in different contexts, such as optics [25], atomic Bose-Einstein condensates [26], and the so-called photonic graphene [27]. This has also led to an interest in this subject from a rigorous mathematical perspective [28]. It is thus quite intriguing that, in principle, 2D balanced CRLH-TL models may host a variety of fundamental effects, such as conical diffraction, formation of topological defects, and even phase transitions, as in Refs. [25–27].

### C. Nonlinear analysis: Coupled NLS equations and solitons

To describe the coupling between a RH and a LH nonlinear mode with equal group velocities, we will use the quasidiscrete approximation, which takes into account the inherent discreteness of the system (see, e.g., Ref. [19] for a review and Refs. [15,23] for relevant recent work). Generally, this approach allows for the description of quasidiscrete envelope solitons (usually satisfying an effective NLS model), characterized by a discrete carrier and a slowly varying continuum envelope. In our case, since we are interested in the description of two different modes, we seek a solution of Eq. (5) in the form

$$V_n = \epsilon \sum_{j=1}^{2} V_j(X,T)\exp(i\theta_j) + \text{c.c.}, \quad (12)$$

where c.c. denotes complex conjugate. In Eq. (12), subscripts $j = 1,2$ correspond to the LH and RH modes, $V_j(X,T)$ are unknown (continuous) slowly varying envelope functions depending on the slow scales $X = \epsilon(n - v_g t)$ (where $v_g$ is the common group velocity) and $T = \epsilon^2 t$, and $\exp(i\theta_j)$, with $\theta_j = k_j n - \omega_j t$, are the (discrete) carriers of frequencies $\omega_j$ and wave numbers $k_j$. Finally, $\epsilon$ is a formal small parameter setting the field amplitude and the slow scales of the envelope functions.

At this point, we should note that the field $V_n$ as expressed in Eq. (12) is in fact the leading-order form of a more general ansatz employing multiple time and space scales. In this context, use of a formal multiscale expansion method leads to a hierarchy of equations at various powers of $\epsilon$, which are solved up to third order. We will present the main results here and provide further details in Appendix A. In particular, from the first- and second-order problems [i.e., at $O(\epsilon)$ (linear limit) and $O(\epsilon^2)$, respectively] we derive the dispersion relation (10) and the group velocity (11). Finally, at the next order, $O(\epsilon^3)$, we obtain the following coupled NLS equations:

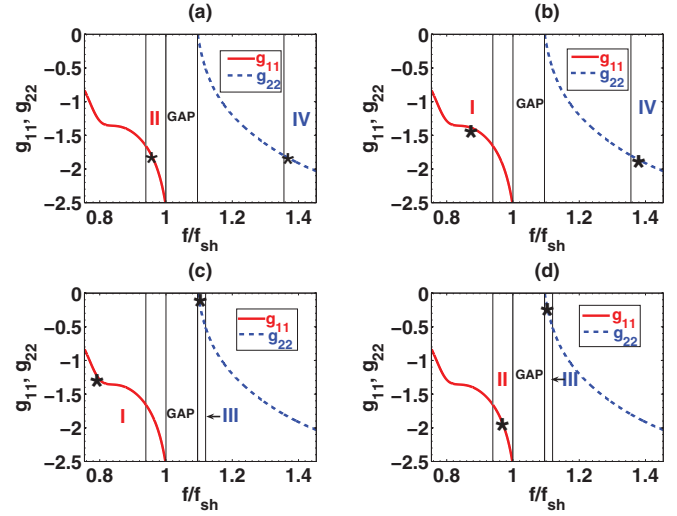$$i\partial_T V_1 + \tfrac{1}{2}D_1\partial_X^2 V_1 + (g_{11}|V_1|^2 + g_{12}|V_2|^2)V_1 = 0, \quad (13)$$



FIG. 4. (Color online) Nonlinearity coefficients $g_{11}$ [solid (red) lines] and $g_{22}$ [dashed (blue) lines] as functions of $f/f_{\text{sh}}$ for interactions in bands (a) II and IV, (b) I and IV, (c) I and III, and (d) II and III. The parameter $\delta$ takes the value $\delta = 1.0954$. Stars (in black) in each panel depict parameter values used in relevant simulations; see Figs. 6 and 7 [corresponding to (a)], Figs. 9 and 10 [corresponding to (b)], Figs. 13 and 14 [corresponding to (c)], and Figs. 15 and 16 [corresponding to (d)] below.

$$i\partial_T V_2 + \tfrac{1}{2}D_2\partial_X^2 V_2 + (g_{21}|V_1|^2 + g_{22}|V_2|^2)V_2 = 0, \quad (14)$$

where the normalized GVD coefficients $D_j$, the self-phase modulation (SPM) coefficients $g_{jj}$, and the cross-phase modulation (CPM) coefficients $g_{j,3-j}$ (with $j = 1,2$) are respectively given by

$$D_j \equiv \frac{\partial^2 \omega_j}{\partial k_j^2} = v_g\left[\cot k_j - \frac{\omega_j^4 + 3\delta^2}{\omega_j(\omega_j^4 - \delta^2)}v_g\right], \quad (15)$$

$$g_{jj} = \frac{\omega_j^3(\omega_j^2 - \delta^2)}{2(\omega_j^4 - \delta^2)}(3\mu - A_j), \quad (16)$$

$$g_{j,3-j} = \frac{\omega_j^3(\omega_j^2 - \delta^2)}{2(\omega_j^4 - \delta^2)}(6\mu - B_{3-j}), \quad (17)$$

where the coefficients $A_j$ and $B_{3-j}$ are defined in Appendix A. It is now useful to remark that for all four possible wave interactions mentioned in the preceding section, the SPM coefficients $g_{jj}$ are negative (see Fig. 4). Then, measuring normalized time $T$ and densities $|V_j|^2$ in units of $|D_1|^{-1}$ and $|D_1/g_{jj}|$, respectively, we express Eqs. (13) and (14) in the following form:

$$i\partial_T V_1 + \frac{s}{2}\partial_X^2 V_1 + (\lambda_1|V_2|^2 - |V_1|^2)V_1 = 0, \quad (18)$$

$$i\partial_T V_2 + \frac{d}{2}\partial_X^2 V_2 + (\lambda_2|V_1|^2 - |V_2|^2)V_2 = 0, \quad (19)$$

where

$$s = \text{sgn}(D_1), \quad d = \frac{D_2}{|D_1|}, \quad \lambda_1 = \frac{g_{12}}{|g_{22}|}, \quad \lambda_2 = \frac{g_{21}}{|g_{11}|}. \quad (20)$$

As seen from Eqs. (18) and (19), in the absence of CPM coupling ($\lambda_j = 0$) the evolution of either the LH mode $V_1$ or the RH mode $V_2$ is described by a single NLS equation. The latter supports soliton solutions of the bright or the dark

type, depending on the sign of dispersion coefficient (see, e.g., Ref. [20]): In particular, the mode $V_1$ ($V_2$) supports bright solitons for $s < 0$ ($d < 0$) or dark solitons for $s > 0$ ($d > 0$). These conditions, however, are modified for $\lambda_j \neq 0$ and various types of coupled (vector) solitons can be found in the full version of Eqs. (18) and (19). Below we will present these types of coupled backward- and forward-propagating solitons belonging, respectively, to the LH low- and RH high-frequency bands.

In principle, four types of vector solitons are possible: bright-bright solitons in the form

$$V_1(X,T) = a_1 \text{sech}(bX) \exp(-i\nu_1 T), \quad (21)$$

$$V_2(X,T) = a_2 \text{sech}(bX) \exp(-i\nu_2 T), \quad (22)$$

BD solitons in the form

$$V_1(X,T) = a_1 \text{sech}(bX) \exp(-i\nu_1 T), \quad (23)$$

$$V_2(X,T) = a_2 \tanh(bX) \exp(-i\nu_2 T), \quad (24)$$

DB solitons in the form

$$V_1(X,T) = a_1 \tanh(bX) \exp(-i\nu_1 T), \quad (25)$$

$$V_2(X,T) = a_2 \text{sech}(bX) \exp(-i\nu_2 T), \quad (26)$$

and DD solitons in the form

$$V_1(X,T) = a_1 \tanh(bX) \exp(-i\nu_1 T), \quad (27)$$

$$V_2(X,T) = a_2 \tanh(bX) \exp(-i\nu_2 T). \quad (28)$$

In the above equations, $a_{1,2}$ and $\nu_{1,2}$ denote the amplitudes and frequencies of each soliton and $b$ is the (common) inverse width of the solitons.

Now, each of the above ansätze is substituted into Eqs. (18) and (19), leading to a set of equations connecting the soliton parameters. In particular, the equations connecting the amplitudes $a_{1,2}$ with the inverse width $b$ are of the form

$$(a_j/b)^2 = -\alpha_j, \quad (29)$$

$$(a_j/b)^2 = (-1)^j \alpha_j, \quad (30)$$

$$(a_j/b)^2 = (-1)^{3-j} \alpha_j, \quad (31)$$

$$(a_j/b)^2 = \alpha_j \quad (32)$$

for the BB, BD, DB, and DD solitons, respectively, where parameters $\alpha_j$ ($j = 1,2$) are given by

$$\alpha_1 = \frac{d\lambda_1 + s}{1 - \lambda_1\lambda_2}, \quad \alpha_2 = \frac{s\lambda_2 + d}{1 - \lambda_1\lambda_2}. \quad (33)$$

In contrast, the frequencies of the BB, BD, DB, and DD solitons are respectively given by

$$\nu_1 = -\frac{s}{2}b^2, \quad \nu_2 = -\frac{d}{2}b^2, \quad (34)$$

$$\nu_1 = -\frac{s}{2}b^2 - \lambda_1 a_1^2, \quad \nu_2 = a_2^2, \quad (35)$$

$$\nu_1 = a_1^2, \quad \nu_2 = -\frac{d}{2}b^2 - \lambda_2 a_2^2, \quad (36)$$

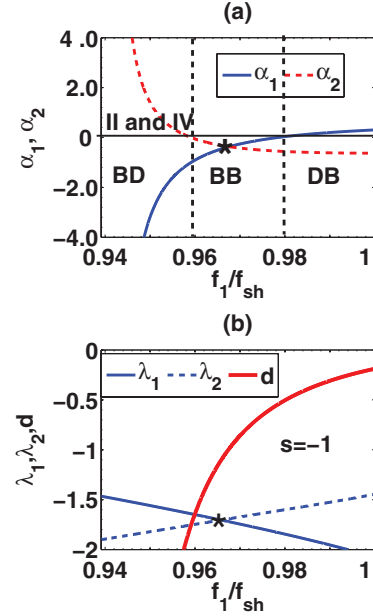$$\nu_1 = a_1^2 - \lambda_1 a_2^2, \quad \nu_2 = a_2^2 - \lambda_2 a_1^2. \quad (37)$$



FIG. 5. (Color online) Parameters for soliton interactions in bands II and IV. (a) Dependence of the coefficients $\alpha_1$ [solid (blue) line] and $\alpha_2$ [dashed (red) line] on the normalized frequency $f_1/f_{\text{sh}}$. (b) Dependence of the parameters $\lambda_1$ [thin solid (blue) line], $\lambda_2$ [dashed (blue) line], and $d$ [bold solid (red) line] on the normalized frequency $f_1/f_{\text{sh}}$.

It is clear that each type of vector soliton is characterized by five independent parameters, connected by a set of four equations; thus each of the above vector solitons is characterized by one free parameter. Furthermore, the fact that the parameters of each soliton component depends on the ones of the other component clearly highlights an important possibility arising from the nonlinear coupling of the solitonic modes: One can control, e.g., the characteristics (amplitude, width, etc.) of a LH soliton by means of the parameters of its RH pair and vice versa.

Requiring that the right-hand sides of Eqs. (29)–(32) are positive, it can be concluded that the existence of each type of vector soliton is determined by the signs of parameters $\alpha_j$: in particular, BB solitons exist for $\alpha_1 < 0$ and $\alpha_2 < 0$, BD solitons exist for $\alpha_1 < 0$ and $\alpha_2 > 0$, DB solitons exist for $\alpha_1 > 0$ and $\alpha_2 < 0$, and DD solitons exist for $\alpha_1 > 0$ and $\alpha_2 > 0$. In contrast, we should mention that the signs of $\alpha_j$ depend on frequency, through the frequency dependence of the parameters involved in Eqs. (33). Thus, for each different type of mode interaction [see cases (i)–(iv) in Sec. II B], below we will present results for the sign (and magnitude) of $\alpha_j$ in bands II and IV, I and IV, I and III, and II and III, and accordingly determine which type of soliton is possible. This way we will show that BB, BD, and DB solitons can exist in certain frequency bands, while DD solitons do not exist: this is due to the fact that $\alpha_1$ and $\alpha_2$ are either of opposite signs or both negative, as attested to by Figs. 5(a), 8, 11, and 12.

Before proceeding with the presentation of the coupled soliton solutions we make the following comments. First, vector solitons will be found in a stationary form; however, using these stationary solutions, one can also find traveling

soliton solutions, with an additional free parameter, i.e., the velocity $C$, by means of the following Galilean boost:

$$V_1(X,T) \rightarrow V_1(X - CT,T)$$
$$\times \exp\left\{\frac{i}{s}\left[CX + \left(\frac{C^2}{2}\right)T\right]\right\}, \quad (38)$$

$$V_2(X,T) \rightarrow V_2(X - CT,T)$$
$$\times \exp\left\{\frac{i}{d}\left[CX + \left(\frac{C^2}{2}\right)T\right]\right\}. \quad (39)$$

Second, it is interesting to note that, contrary to what is often the case in the mathematically studied multicomponent variants of the NLS equation [21], the model of Eqs. (18) and (19) does not necessarily respect the condition $\lambda_1 = \lambda_2$. The latter condition ensures the existence of an underlying Hamiltonian structure and is customary in other physical applications (such as atomic physics [29]). Nevertheless, as we will see below, this is not a necessary condition for the existence of the exact soliton solutions considered below.

## III. SOLITON INTERACTIONS IN DIFFERENT FREQUENCY BANDS: NUMERICAL RESULTS

### A. Numerical procedure

Let us now proceed to study numerically the evolution of the coupled solitons presented in the previous section in the framework of the fully discrete model of Eq. (5). In order to compare the analytical approximations with the results of numerical simulations, we will make use of two diagnostic quantities: The first one is the evolution of the center of mass defined as

$$X(t) = \frac{\sum_{n=-N}^{n=N} n V_n^2}{\sum_{n=-N}^{n=N} V_n^2} \quad (40)$$

and the second one is a powerlike quantity defined as

$$P(t) = \sum_{n=-N}^{n=N} V_n^2, \quad (41)$$

with $2N + 1$ being the lattice size. The above quantities can readily be determined for each type of vector soliton that is predicted analytically in the framework of the coupled NLS equations.

In all simulations, which have been performed by means of a fixed-step fourth-order Runge-Kutta scheme with a time step equal to 0.01, we have fixed the value of the small parameter as $\epsilon = 0.02$ and we have used periodic boundary conditions. Use of the latter leads to the requirement that the wave number $k$ of a dark soliton component must be equal to $2\pi q/p$, with $q, p \in \mathbb{Z}$ and $q$ also being odd.

In all figures below (Figs. 6–16), unless stated otherwise, we show the density plots of $V_n$, the spatial profile of $V_n$ at $t = 2000$, the time evolution of the center of mass $X(t)$ and the quantity $P(t)$.

Regarding the evolution time of the simulations, we should note the following. Most of our simulations are performed for relatively large normalized times, typically up to $t \sim 10^7$ in some cases. However, given our time normalization, the physical unit time (set by the frequency $f_{sh} = 14.529$ GHz)
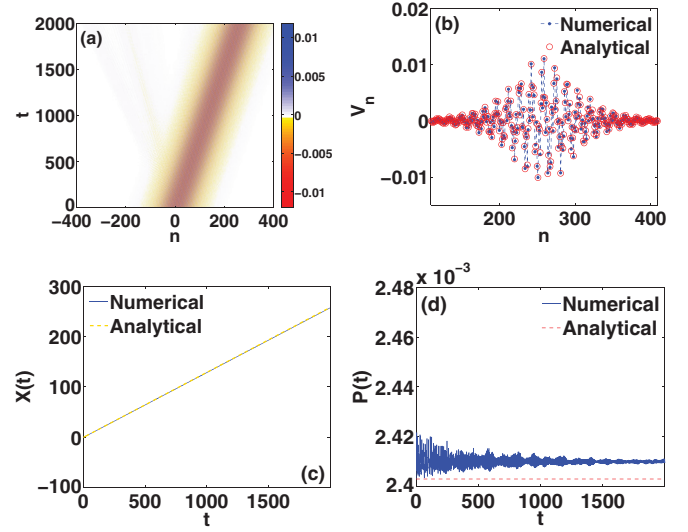


FIG. 6. (Color online) Bright-bright solitons in regions II–IV. (a) Density plot of the space-time evolution of $V_n$ obtained numerically. (b) Comparison of the analytical and numerical profiles of $V_n$ at $t = 2000$. Also shown is the time evolution of (c) the center of mass and (d) the power diagnostic. The parameters used are $f_1/f_{sh} = 0.96545$ and $f_2/f_{sh} = 1.36535$, which give $k_1 = -0.4061$ and $k_2 = 1.8576$, i.e., a bright-bright soliton in bands II and IV (this particular choice corresponds to the points depicted by stars in Fig. 5). The difference in the powers can be attributed to the approximate nature of our solution.

is very small, namely, $t_0 = (2\pi f_{sh})^{-1} \approx 11$ ps (see Sec. II A). Actually, since all characteristic frequencies of the system [see Eq. (7)] are in the microwave regime, all characteristic times are less than a nanosecond and thus, obviously, simulations for time $t$ even of the order of $10^9$ are extremely time consuming. Nevertheless, our results for normalized times up to $t = 10^7$
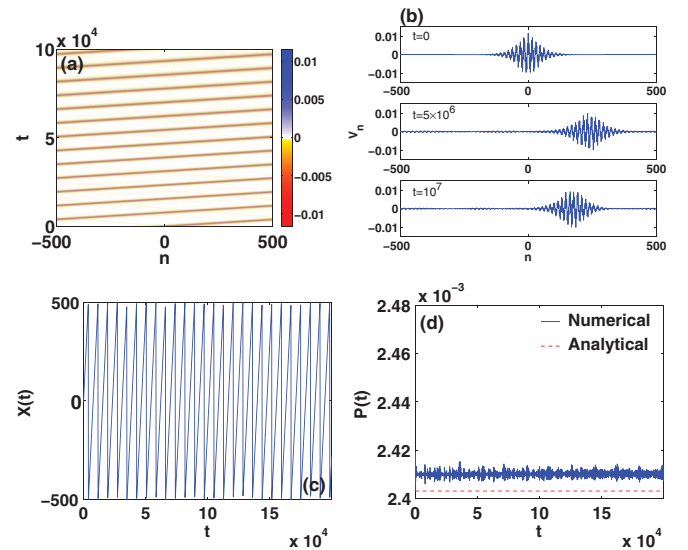


FIG. 7. (Color online) The bright-bright soliton of Fig. 6 evolves until $t = 10^5$. All the panels are similar to those of Fig. 6 except for (b), in which snapshots of the soliton at $t = 5 \times 10^6$ and $t = 10^7$ are compared to the initial condition of the simulation in order to examine its robustness under a very long evolution time.
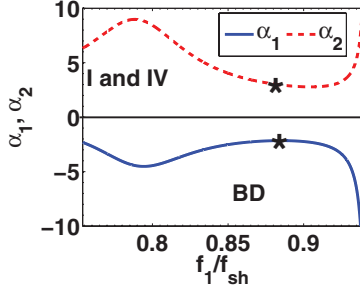
FIG. 8. (Color online) Parameters for solitons in bands I and IV. Shown is the dependence of the coefficients $\alpha_1$ [solid (blue) line] and $\alpha_2$ [dashed (red) line] on the normalized frequency $f_1/f_{sh}$. Stars depict parameter values used for the simulations shown in Figs. 9 and 10 below.

(corresponding to a physical time of the order of one-tenth of a millisecond) demonstrate good agreement with our analytical predictions in suitable cases (see below). Furthermore, the results of such long simulations can also be used as a reliable indication of the solitons' robustness. Hence, in the case where the solitary waves are found to be very robust, we expect that they would survive for the longer time scales that would render them experimentally observable.

### B. BD, BB, and DB solitons in bands II and IV

First, we consider the interaction between a backward-propagating soliton, with a frequency lying in band II, and a forward-propagating soliton, with a frequency lying in band IV (for $\delta = 1.0954$). In this case, $s = -1$ (see Fig. 3) and, following the analysis of the previous section, we find three different types of vector solitons in certain subbands.
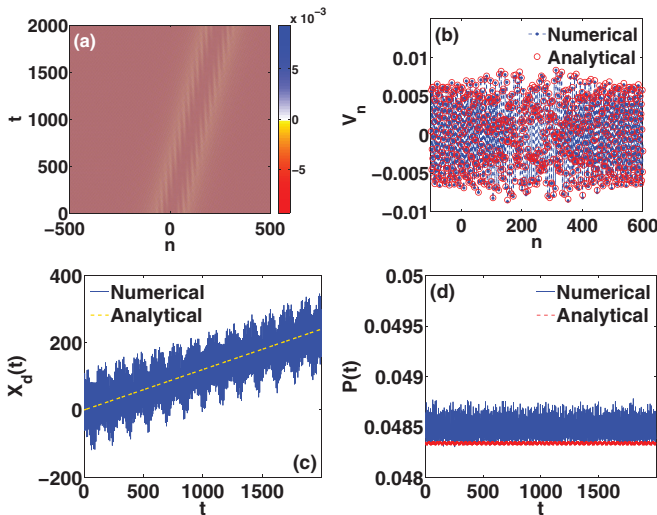


FIG. 9. (Color online) Bright-dark solitons in regions I and IV. (a) Density plot of the time evolution of $V_n$ obtained numerically. (b) Comparison of the analytical and numerical profiles of $V_n$ at $t = 2000$. Also shown is the time evolution of (c) the center of mass and (d) the power diagnostics. The parameters used are $f_1/f_{sh} = 0.8831$ and $k_2 = 5\pi/8 \approx 1.9625$, which give $k_1 = -1.0404$ and $f_2/f_{sh} = 1.3748$ (see the corresponding points depicted by stars in Fig. 8), i.e., a bright-dark soliton in bands I and IV.
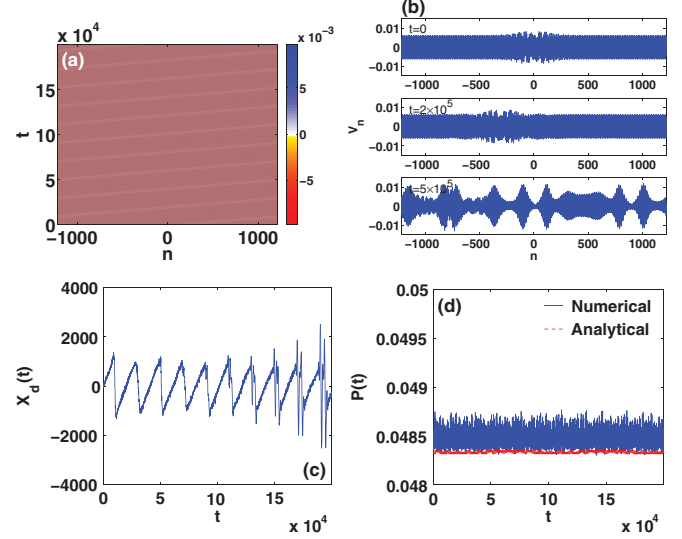


FIG. 10. (Color online) The bright-dark soliton of Fig. 9 evolves until $t = 2 \times 10^5$. All the panels are similar to those of Fig. 9 except for (b), in which snapshots of the soliton at $t = 2 \times 10^5$ and $t = 5 \times 10^5$ are compared to the initial condition of the simulation. Notice that the center of mass is not bounded in $[-N, N]$; this can be caused by the soliton splitting. In this setting, the modulational instability of the background (see the discussion in Appendix B) appears to be responsible for the breakup of the wave packet.

(i) If $0.94 < f_1/f_{sh} < 0.96$ then $\alpha_1 < 0$ and $\alpha_2 > 0$; thus BD solitons exist, with the frequency of the bright (dark) soliton component being in the LH low- (RH high-) frequency band.

(ii) If $0.96 < f_1/f_{sh} < 0.98$ then $\alpha_1 < 0$ and $\alpha_2 < 0$; thus BB solitons exist, with the soliton frequencies being one in the LH low- and one in the RH high-frequency band.

(iii) If $0.98 < f_1/f_{sh} < 1$ then $\alpha_1 > 0$ and $\alpha_2 < 0$; thus DB solitons exist, with the frequency of the dark (bright) soliton being in the LH low- (RH high-) frequency band.

Here we will focus on the BB soliton case (BD and DB solitons will be studied below). In particular, we will investigate the dynamics of a BB soliton corresponding to the frequency value $f_1/f_{sh} = 0.965$: For this value, the dispersion coefficient $d$ becomes $d \simeq -1 = s$, the CPM coefficients $\lambda_{1,2}$ take the values $\lambda_1 = \lambda_2 = \lambda = -1.7$, and $\alpha_1 = \alpha_2 = 0.487$ (see the intersection point of the relevant curves depicted by a star in Fig. 5). In this case, the BB soliton has a (common
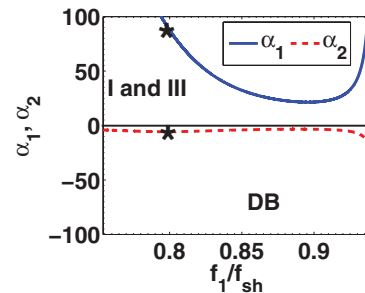


FIG. 11. (Color online) Same as Fig. 8, but for soliton interactions in bands I and III. Stars depict parameter values used for the simulations shown in Figs. 13 and 14 below.
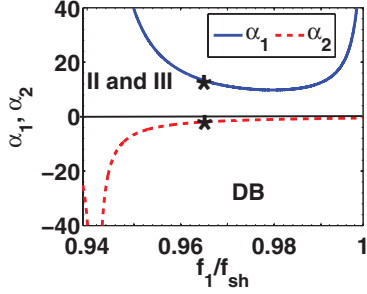
FIG. 12. (Color online) Same as Fig. 8, but for soliton interactions in bands II and III. Stars depict parameter values used for the simulations shown in Figs. 15 and 16 below.

for both components) group velocity $v_g = 0.1288$, which occurs when the (normalized) carrier frequencies for the modes $V_1$ and $V_2$ take, respectively, the values $f_1/f_{sh} = 0.965$ (as mentioned above) and $f_2/f_{sh} = 1.365$. Notice that other BB soliton solutions not obeying the above particular conditions ($\lambda_1 = \lambda_2$ and $d = -1$) exist as well, as per our analysis of the previous section.

At this point, we should mention that this choice of the parameter values leads to symmetric coupled NLS equations (18) and (19) (and also to symmetric BB solitons of equal amplitudes; see, e.g., Ref. [30]). A very interesting subcase, corresponding to $\lambda = -1$ (i.e., equal SPM and CPM coefficients), would render Eqs. (18) and (19) the completely integrable Manakov system [31]; in such a case, in Fig. 5(b), the curve for parameter $d$ would intersect the curves for $\lambda_{1,2}$, with all parameters taking the value $-1$. However, we have checked that other, physically relevant, choices of the values of the parameter $\delta$ do not lead to the Manakov case [the chosen
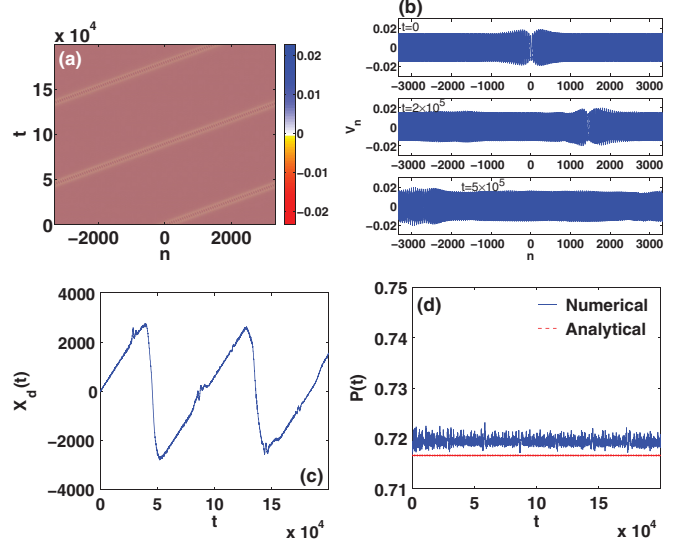


FIG. 14. (Color online) The dark-bright soliton of Fig. 13 evolves until $t = 2 \times 10^5$. All the panels are similar to those of Fig. 13 except for (b), in which snapshots of the soliton at $t = 2 \times 10^5$ and $t = 5 \times 10^5$ are compared to the initial condition of the simulation in order to examine its robustness under a very lengthy time evolution.

value $\delta = 1.0954$ only leads to symmetric NLS equations (18) and (19)].

Utilizing the above-mentioned BB soliton solution, we can express the voltage $V_n(t)$ in Eq. (5) in terms of the original coordinates $n$ and $t$ as follows:

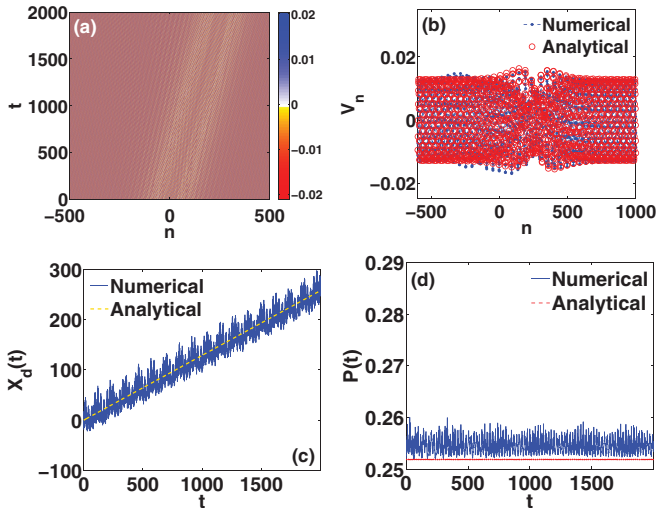$$V_n(t) \approx V_0[R_1(n,t)\cos(k_1 n - \Omega_1 t) + R_2(n,t)\cos(k_2 n - \Omega_2 t)], \quad (42)$$



FIG. 13. (Color online) Dark-bright solitons in regions I and III. (a) Density plot of the time evolution of $V_n$ obtained numerically. (b) Comparison of the analytical and numerical profiles of $V_n$ at $t = 2000$. Also shown is the time evolution of (c) the center of mass and (d) the width diagnostic. The parameters used are $k_1 = -6\pi/5 \approx -1.884$ and $f_2/f_{sh} = 1.1002$, which give $f_1/f_{sh} = 0.8003$ and $k_2 = 0.1232$ (cf. points depicted by stars in Fig. 11), i.e., a dark-bright soliton in bands I and III.
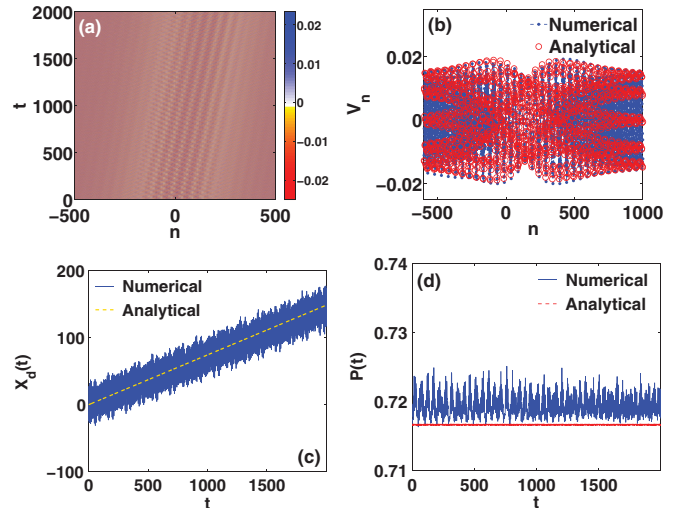


FIG. 15. (Color online) Dark-bright solitons in regions II and III. (a) Density plot of the time evolution of $V_n$ obtained numerically. (b) Comparison of the analytical and numerical profiles of $V_n$ at $t = 2000$. Also shown is the time evolution of (c) the center of mass and (d) the width diagnostic. The parameters used are $k_1 = -3\pi/23 \approx -0.4095$ and $f_2/f_{sh} = 1.1162$, which give $f_1/f_{sh} = 0.965$ and $k_2 = 0.2758$ (cf. stars in Fig. 12), i.e., a dark-bright soliton in bands II and III.

where functions $R_1$ and $R_2$ have the following form:

$$R_1 = \text{sech}[\sqrt{2\ell}\epsilon(n - v_g t)], \tag{43}$$

$$R_2 = \sqrt{\left|\frac{g_{11}}{g_{22}}\right|} \, \text{sech}[\sqrt{2\ell}\epsilon(n - v_g t)]. \tag{44}$$

In the above equations, $\ell$ is an arbitrary parameter, while the solution amplitude $V_0$ and the frequencies $\Omega_j$ $(j = 1,2)$ are given by

$$V_0 = 2\epsilon\sqrt{\left|\frac{D_1}{g_{11}}\right| \frac{2\ell}{1 - \lambda}}, \quad \Omega_j = \omega_j + \epsilon^2\ell|D_1|, \tag{45}$$

with $\omega_j \equiv f_j/f_{\text{sh}}$. Now, substituting Eq. (42) into Eqs. (40) and (41), we obtain (for sufficiently small $\epsilon$) our diagnostic quantities

$$X(t) = v_g t, \quad P(t) = \frac{V_0^2}{\epsilon\sqrt{2\ell}}\left(1 + \left|\frac{g_{11}}{g_{22}}\right|\right). \tag{46}$$

In Figs. 6 and 7 we show the outcome of the simulations for short and long times, respectively, of a bright-bright soliton with $\ell = 1$ and $N = 500$. The parameters used are $f_1/f_{\text{sh}} = 0.965$ and $f_2/f_{\text{sh}} = 1.365$, which give $k_1 = -0.406$ and $k_2 = 1.857$. In Fig. 6 it is evident that the agreement between analytical and numerical results pertaining to the soliton profile, as well as the evolution of the center of mass and power diagnostics, is very good. In the case shown in Fig. 7 we have performed a very long simulation, up to normalized times $t = 10^7$. It is clear that that the initial pulse does not spread out, which indicates the soliton robustness: Figs. 7(a) and 7(b), in particular the snapshots of the pulse profile at
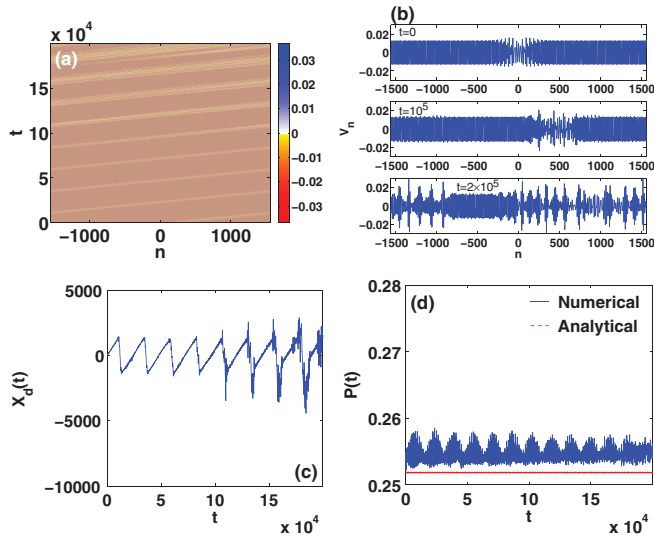


FIG. 16. (Color online) The dark-bright soliton of Fig. 15 evolves until $t = 2 \times 10^5$. All the panels are similar to those of Fig. 15 except for (b), in which snapshots of the soliton at $t = 10^5$ and $t = 2 \times 10^5$ are compared to the initial condition of the simulation. Notice that, as in Fig. 10, the center of mass is not bounded in $[-N,N]$, as in that case, the soliton splits at long evolution times. In this setting too, as per the analysis of Appendix B, the modulational instability of the background appears to be responsible for the breakup of the wave packet.

$t = 10^7$, clearly show that the soliton persists as a stable object up to the end of this long simulation time. We note in passing that a fragment of the soliton is backscattered when the soliton starts its motion at $t = 0$ (due to the approximate nature of our analytical solution profile). Notice that despite this emission and the subsequent interaction of the fragment with the "distilled" solitary wave, the coherent structure remains robust and preserves its characteristics throughout the evolution thereafter.

### C. BD solitons in bands I and IV

Next we consider the interaction between a backward-propagating soliton, with a frequency in band I, and a forward-propagating soliton, with a frequency in band IV; in this case, $s = 1$ (see Fig. 3). In Fig. 8 we show the dependence of the parameters $\alpha_1$ and $\alpha_2$ on the normalized frequency $f_1/f_{\text{sh}}$ (for $\delta = 1.0954$). It is observed that $\alpha_1 < 0$ and $\alpha_2 > 0$ and thus solely BD solitons exist in bands I and IV.

Employing the solutions (23) and (24), we can again approximate a solution of Eq. (5) for the voltage $V_n(t)$, in terms of the original coordinates $n$ and $t$, as follows:

$$\begin{aligned} V_n(t) \approx V_0[\Psi_1(n,t)\cos(k_1 n - \Omega_1 t) \\ + \Psi_2(n,t)\cos(k_2 n - \Omega_2 t)], \end{aligned} \tag{47}$$

where

$$\Psi_1 = \sqrt{-\frac{\alpha_1}{\alpha_2}} \, \text{sech}[\epsilon b(n - v_g t)], \tag{48}$$

$$\Psi_2 = \sqrt{\left|\frac{g_{11}}{g_{22}}\right|} \, \tanh[\epsilon b(n - v_g t)]. \tag{49}$$

In this case, the solution amplitude $V_0$ and the frequencies $\Omega_j$ $(j = 1,2)$ are given by

$$V_0 = 2\epsilon\sqrt{v_2\left|\frac{D_1}{g_{11}}\right|}, \quad \Omega_j = \omega_j + \epsilon^2 v_j|D_1|. \tag{50}$$

In order to get an expression for the center of mass similar to that of the bright-bright soliton (46), we must define it as

$$X_d(t) = \frac{F(t)X(t)}{\Psi_{1,0}^2 - \Psi_{2,0}^2} - \frac{\epsilon bN}{2}\Psi_{2,0}^2\cot(k_2)\sin(2\Omega_2 t), \tag{51}$$

where

$$F(t) = \Psi_{1,0}^2 + \Psi_{2,0}^2(\epsilon bN - 1) + \frac{\epsilon b}{2}\Psi_{2,0}^2[1 - \cos(2\Omega_2 t)]. \tag{52}$$

Substituting Eq. (47) into Eqs. (41) and (51) we can once again obtain relevant expressions (provided $\epsilon$ is small enough) for the center of mass and power:

$$X_d(t) = v_g t, \quad P_d(t) = \frac{V_0^2}{\epsilon b}F(t). \tag{53}$$

Figures 9 and 10 show the evolution of a BD soliton (and its characteristics) in bands I and IV with $v_2 = 1$ and $N = 1220$. The parameters used are $f_1/f_{\text{sh}} = 0.8831$ and $k_2 = 5\pi/8 \approx 1.9625$, which give $k_1 = -1.0404$ and $f_2/f_{\text{sh}} = 1.3748$. In this case, it is clear that although BD solitons do exist, the agreement between analytical and numerical results becomes

worse over time. Also, as shown in Fig. 10(b), the pulse profile indicates that the BD soliton is not a robust object. The observed long-time behavior of the BD soliton can be attributed to the fact that the background of the dark soliton component, namely, a continuous wave (cw), is subject to the modulational instability (see Refs. [18,24]). This point is explained in more detail in Appendix B.

### D. DB solitons in bands I-III and II-III

Finally, we consider the cases of coupled solitons in bands I and III, as well as in bands II and III. In both cases, as is observed in Figs. 11 (bands I and III) and 12 (bands II and III), we find that $\alpha_1 > 0$ and $\alpha_2 < 0$ and thus solely DB solitons exist in these bands. Following our previous considerations, we may use the DB soliton solutions of Eqs. (25) and (26) and approximate the voltage $V_n(t)$ in Eq. (5), in terms of the original coordinates, as follows:

$$V_n(t) = V_0[\Phi_1(n,t)\cos(k_1 n - \Omega_1 t) + \Phi_2(n,t)\cos(k_2 n - \Omega_2 t)], \quad (54)$$

where functions $\Phi_1$ and $\Phi_2$ are given by

$$\Phi_1 = \tanh[\epsilon B(n - v_g t)], \quad (55)$$

$$\Phi_2 = \sqrt{-\frac{\alpha_2}{\alpha_1}\left|\frac{g_{11}}{g_{22}}\right|}\,\text{sech}[\epsilon B(n - v_g t)], \quad (56)$$

while the rest of the soliton parameters are

$$V_0 = 2\epsilon\sqrt{\nu_1\left|\frac{D_1}{g_{11}}\right|}, \quad \Omega_j = \omega_j + \epsilon^2 \nu_j |D_1|. \quad (57)$$

Figures 13 and 14 show the outcome of the simulations for a DB soliton in bands I and III (with $\nu_1 = 3$ and $N = 3333$), while Figs. 15 and 16 correspond to a DB soliton in bands II and III (with $\nu_1 = 3$ and $N = 1553$). The parameters used are $k_1 = -6\pi/5 \approx -1.884$ and $f_2/f_{\text{sh}} = 1.1002$, which give $f_1/f_{\text{sh}} = 0.8003$ and $k_2 = 0.1232$, in bands I and III, and $k_1 = -3\pi/23 \approx -0.4095$ and $f_2/f_{\text{sh}} = 1.1162$, which give $f_1/f_{\text{sh}} = 0.965$ and $k_2 = 0.2758$, in bands II and III, respectively. In the latter case, the relatively large values of the number of particles and of $\nu_1$ used are motivated by the necessity of a vanishing tail for the bright component at the edges of the lattice. As seen in this set of figures, DB solitons in bands II and III and bands I and III do exist, as predicted in theory. Furthermore, it is observed that the former are less robust than the latter, as seen both from their stronger deformation and the fact that they lose their solitary-wave character earlier. In fact, as observed in Fig. 16(b) and explained in Appendix B, the cw background of the dark soliton is subject to the modulation instability, as in the case of interactions in bands I and IV. On the contrary, DB solitons in bands I and III seem to essentially preserve their structure even in the long evolution of Fig. 14; in this case, as also explained in Appendix B, the cw background carrying the dark soliton is modulationally stable. This fact can, at least qualitatively, explain the different long-time behavior of the DB solitons observed in Figs. 16 and 14 and the fact that DB solitons in bands I and III are more robust than the ones in bands II and III.

## IV. CONCLUSION

We have used both analytical and numerical techniques to study the existence and dynamical robustness of coupled backward- and forward-propagating solitons in a composite right- and left-handed nonlinear transmission line. The considered form of the TL was a quite generic one, finding applications to the modeling of a wide range of LH systems and devices, with parasitic RH behavior, such as resonators, antennas, and directional couplers [1–4].

Our analysis started with the derivation of a nonlinear lattice equation governing the voltage across the fundamental (unit-cell) element of the transmission line. In the linear regime, we derived the dispersion relation for small-amplitude linear plane waves and showed that they may propagate in either a right-handed high-frequency region or a left-handed low-frequency region. We also identified frequency bands where RH and LH modes can propagate with the same group velocity.

Using the above result, we then investigated the possibility of nonlinearity-assisted coupling between LH and RH modes. This way, in order to analytically treat the nonlinear lattice equation, we used the so-called quasidiscrete approximation. The latter is a variant of the multiscale perturbation method, which takes into account the discreteness of the system by considering the carrier (envelope) of the wave as a discrete (continuum) function of space. Employing this approach, we derived, in the small-amplitude approximation and for certain space and time scales, a system of two coupled nonlinear Schrödinger equations for the unknown voltage envelope functions. This system was then used to predict the existence of coupled backward- and forward-propagating solitons of the bright-bright, bright-dark, and dark-bright types, respectively. Importantly, the analysis of such a nonlinear coupling suggests that it is possible to control the characteristics (amplitude, width, etc.), e.g., of a LH soliton with the ones of a RH soliton.

The above-mentioned existence results, as well as the propagation properties and the potential robustness of these vector solitons, were then investigated for each of the possible scenarios. This was done by means of direct numerical simulations of the full CRLH-TL nonlinear lattice model, using as initial conditions the analytical forms of solitons predicted by the perturbation theory. In the simulations, apart from the evolution of the shape, we also studied the evolution of the center of mass and a powerlike quantity of the various solitons. Our numerical results have confirmed the existence of the various types of solitons predicted analytically, but have also revealed their distinct robustness characteristics. In particular, we found that bright-bright solitons feature a robust propagation over long times. In contrast, as concerns solitons of the mixed type (namely, dark-bright and bright-dark ones), we found that in specific frequency bands (bands I and III), dark-bright solitons are more robust than those in other bands (i.e., II and III) or bright-dark solitons: Dark-bright solitons in bands II and III and bright-dark solitons preserve their shape only for finite times and for sufficiently long evolutions they are either destroyed (bright-dark) or are significantly deformed (dark-bright). A qualitative explanation of the above behavior may be attributed to the fact that the continuous-wave background of the dark soliton was found

to be, in the effective NLS picture, modulationally stable (unstable) in bands I and III (bands I and IV and bands II and III).

We can thus postulate that from all types of solitons predicted analytically, bright-bright and dark-bright ones (in bands I and III) are the most likely ones to be experimentally observable. In all cases, our numerical results were found to corroborate the analytical predictions, at least up to the times during which the solitary waves propagate robustly.

It would be interesting to study other types of nonlinear CRLH-TL lattice models modeling realistic structures composed by LH metamaterials. In that regard, a pertinent interesting direction would be the investigation of the effects of damping and driving, which may lead to robust nonlinear waveforms, which would constitute dynamical attractors in such settings. Additionally, the study of higher-dimensional settings is a particularly challenging problem. In the latter context, in addition to simpler (yet genuinely higher-dimensional or even quasi-one-dimensional) solitary-wave structures, more complex waveforms, such as vortices, may be realizable.

## ACKNOWLEDGMENTS

## APPENDIX A: PERTURBATION SCHEME

Our analytical approximation relies on the use of the quasicontinuum approximation, which is a variant of the method of multiple scales [32]. We introduce independent temporal variables $t_m = \epsilon^m t$ ($m = 0, 1, 2, \ldots$) and accordingly expand the time derivative operator as $\partial_t = \partial_{t_0} + \epsilon \partial_{t_1} + \cdots$. Next we seek solutions of Eq. (5) in the form

$$V_n = \sum_{m=1} \epsilon^m u_{mn}(t_m) + \text{c.c.} \tag{A1}$$

(recall that subscript $n$ denotes the lattice site). Then we substitute Eq. (A1) into Eq. (5) and employ a continuum approximation for functions $u_{mn}$, i.e., $u_{mn} \to u_m(x)$, where $x = nh$ and $h$ is the lattice spacing (the latter parameter does not appear in the results below, as one may readily rescale $x$ as $x/h$). Furthermore, we introduce the spatial variables $x_m = \epsilon^m x$ and thus $\partial_x = \partial_{x_0} + \epsilon \partial_{x_1} + \cdots$.

We now seek a solution in the form

$$u_1 = \sum_{j=1}^{2} V_j(x_1, x_2, \ldots, t_1, t_2, \ldots) \exp(i\theta_j) + \text{c.c.}, \tag{A2}$$

where subscripts $j = 1$ and 2 correspond to the LH low- and RH high-frequency bands, $V_j$ is an unknown complex envelope function, $\theta_j = k_j x_0 - \omega_j t_0$, and the wave numbers $k_j$ and frequencies $\omega_j$ satisfy the dispersion relation (10). Substituting Eq. (A2) into Eq. (5) and equating coefficients of like powers

of $\epsilon$, we obtain the (first three) perturbation equations

$$\hat{L}_0 u_1 = 0 \quad \text{for } O(\epsilon), \tag{A3}$$

$$\hat{L}_0 u_2 + \hat{L}_1 u_1 + \hat{N}_0 u_1^2 = 0 \quad \text{for } O(\epsilon^2), \tag{A4}$$

$$\hat{L}_1 u_2 + \hat{L}_2 u_1 + \hat{N}_0 [u_1 u_2 + \mu u_1^3] = 0 \quad \text{for } O(\epsilon^3), \tag{A5}$$

where the operators are given by

$$\hat{L}_0 = \frac{\partial^4}{\partial t_0^4} + \left(1 + \delta^2 + 4\beta^2 \sin^2 \frac{k_j}{2}\right) \frac{\partial^2}{\partial t_0^2} + \delta^2, \tag{A6}$$

$$\hat{L}_1 = 4\frac{\partial^4}{\partial t_0^3 \partial t_1} + 2\left(1 + \delta^2 + 4\beta^2 \sin^2 \frac{k_j}{2}\right) \frac{\partial^2}{\partial t_0 \partial t_1}$$
$$- 2i\beta^2 \sin k_j \frac{\partial^3}{\partial t_0^3 \partial x_1}, \tag{A7}$$

$$\hat{L}_2 = \left(1 + \delta^2 + 4\beta^2 \sin^2 \frac{k_j}{2}\right)\left(\frac{\partial^2}{\partial t_1^2} + 2\frac{\partial^2}{\partial t_0 \partial t_2}\right)$$
$$- 6\frac{\partial^4}{\partial t_0^2 \partial t_1^2} + 4\frac{\partial^4}{\partial t_0^3 \partial t_2}\beta^2 \cos k_j \frac{\partial^4}{\partial t_0^2 \partial x_1^2}$$
$$- 4i\beta^2 \sin k_j \frac{\partial^3}{\partial t_0 \partial t_1 \partial x_1} - 2i\beta^2 \sin k_j \frac{\partial^4}{\partial t_0^2 \partial x_2^2}, \tag{A8}$$

$$\hat{N}_0 = \left(\frac{\partial^4}{\partial t_0^4} + \delta^2 \frac{\partial^2}{\partial t_0^2}\right). \tag{A9}$$

Next, substituting Eq. (A2) into Eq. (A4), we obtain the nonsecularity condition

$$\frac{\partial V_j}{\partial t_1} + \left[\frac{\omega_j \beta^2 \sin k_j}{2\omega_j^2 - \left(1 + \delta^2 + 4\beta^2 \sin^2 \frac{k_j}{2}\right)}\right]\frac{\partial V_j}{\partial x_1} = 0, \tag{A10}$$

which suggests that $V_j = V_j(X, x_2, \ldots, t_2, \ldots)$, where $X = x_1 - v_{g_j} t_1$, while the group velocities $v_{g_j}$ result self-consistently as $v_{g_j} = \partial \omega_j / \partial k_j$ [cf. Eq. (11)]. Employing Eq. (A10), we may determine from Eq. (A4) the unknown field $u_2$,

$$u_2 = -\sum_{j=1}^{2} \frac{4\omega_j^2(4\omega_j^2 - \delta^2)}{G_j(2\omega_j, 2k_j)} V_j^2 \exp(i2\theta_j)$$
$$- \frac{2[(\omega_1 + \omega_2)^4 - \delta^2(\omega_1 + \omega_2)^2]}{G_3(\omega_1 + \omega_2, k_1 + k_2)} V_1 V_2 \exp[i(\theta_1 + \theta_2)]$$
$$- \frac{2[(\omega_1 - \omega_2)^4 - \delta^2(\omega_1 - \omega_2)^2]}{G_4(\omega_1 - \omega_2, k_1 - k_2)} V_1 V_2^* \exp[i(\theta_1 - \theta_2)]$$
$$- \sum_{j=1}^{2} F_j(x_1, x_2, \ldots, t_1, t_2, \ldots) + \text{c.c.}, \tag{A11}$$

where functions $G_j(\omega_j, k_j)$ ($j = 1, 2$) are given by:

$$G_j = -(1 + \delta^2 + 4\beta^2 \sin^2 k_j)(2\omega_j)^2$$
$$+ (2\omega_j)^4 + \delta^2, \tag{A12}$$

$$G_3 = -\left[1 + \delta^2 + 4\beta^2 \sin^2\left(\frac{k_1 + k_2}{2}\right)\right](\omega_1 + \omega_2)^2$$
$$+ (\omega_1 + \omega_2)^4 + \delta^2, \tag{A13}$$

$$G_4 = -\left[1 + \delta^2 + 4\beta^2 \sin^2\left(\frac{k_1 - k_2}{2}\right)\right](\omega_1 - \omega_2)^2$$
$$+ (\omega_1 - \omega_2)^4 + \delta^2. \qquad (A14)$$

In contrast, functions $F_j(x_1, x_2, \ldots, t_1, t_2, \ldots)$ can be derived at $O(\epsilon^4)$ by means of the equation

$$\hat{L}_2 u_2 + \hat{N}_2 u_1^2 = 0, \qquad (A15)$$

which leads to the result

$$F_j = -\frac{2\omega_j^2 \delta^2}{\omega_j^4 + \delta^2}. \qquad (A16)$$

To this end, we arrive at the following expression for $u_2$:

$$u_2 = -\sum_{j=1}^{2} c_j V_j^2 \exp(i2\theta_j) - c_3 V_1 V_2 \exp[i(\theta_1 + \theta_2)]$$
$$- c_4 V_1 V_2^* \exp[i(\theta_1 - \theta_2)] - \sum_{j=1}^{2} c_{0j}|V_j|^2 + \text{c.c.},$$
$$(A17)$$

where

$$c_j = \frac{4\omega_j^2\left(4\omega_j^2 - \delta^2\right)}{G_j(2\omega_j, 2k_j)}, \qquad (A18)$$

$$c_3 = \frac{2[(\omega_1 + \omega_2)^4 - \delta^2(\omega_1 + \omega_2)^2]}{G_3(\omega_1 + \omega_2, k_1 + k_2)}, \qquad (A19)$$

$$c_4 = \frac{2[(\omega_1 - \omega_2)^4 - \delta^2(\omega_1 - \omega_2)^2]}{G_4(\omega_1 - \omega_2, k_1 - k_2)}, \qquad (A20)$$

$$c_{0j} = \frac{2\omega_j^2 \delta^2}{\omega_j^4 + \delta^2}. \qquad (A21)$$

Finally, defining the coefficients

$$A_j = c_{0j} + c_j, \qquad (A22)$$

$$B_{3-j} = c_{03-j} + c_3 + c_4 \qquad (A23)$$

and using the variables $X = x_1 - v_g t_1 \equiv \epsilon(n - v_g t)$ and $T = t_2 \equiv \epsilon^2 t$, we derive from the nonsecularity condition at $O(\epsilon^3)$ the coupled NLS equations (18) and (19).

## APPENDIX B: MODULATIONAL INSTABILITY

In this Appendix we provide results for the modulational instability of plane wave solutions of Eqs. (18) and (19) (details can be found, e.g., in Refs. [18,24]). First we note that Eqs. (18) and (19) possess exact cw solutions, of constant amplitudes

$V_{j(0)}$, of the form

$$V_j = V_{j(0)} \exp(-i\varphi_j), \qquad (B1)$$

where $\varphi_j = (V_{j(0)}^2 - \lambda_j V_{3-j,(0)}^2)T$ (with $j = 1,2$). The stability of the above cw solutions is studied by introducing the following ansatz into Eqs. (18) and (19):

$$V_j = (V_{j(0)} + \psi_j)\exp(i\varphi_j), \qquad (B2)$$

where $\psi_j$ is a small perturbation. Then, linearizing the resulting equations with respect to $\psi_j$ and assuming that

$$\psi_j = p_j \cos(K_p X - \Omega_p T) + iq_j \sin(K_p X - \Omega_p T), \quad (B3)$$

where $K_p$ and $\Omega_p$ are the wave number and the frequency of perturbation, we derive a homogeneous system of four equations for the perturbation amplitudes $p_j$ and $q_j$. Requiring that the system admits a nontrivial solution, we derive the following dispersion relation for $\Omega_p$ and $K_p$:

$$\Omega_p^4 - (\rho_1 + \rho_2)\Omega_p^2 + \rho_1\rho_2 - \gamma = 0, \qquad (B4)$$

where

$$\rho_1 = \frac{sK_p^2}{2}\left(\frac{sK_p^2}{2} + 2V_{1(0)}^2\right), \qquad (B5)$$

$$\rho_2 = \frac{dK_p^2}{2}\left(\frac{dK_p^2}{2} + 2V_{2(0)}^2\right), \qquad (B6)$$

$$\gamma = sd\lambda_1\lambda_2 V_{1(0)}^2 V_{2(0)}^2. \qquad (B7)$$

A general study of Eq. (B4) is provided in Ref. [24]. Here we may study a simpler case, where solely one cw (which carries a dark soliton) is present (i.e., $\gamma = 0$), so as to explain the long-time behavior of BD and DB solitons observed in simulations. In this case, if $\rho_1\rho_2 < 0$ then the cw is modulationally unstable because $\text{Im}\{\Omega_p\} \neq 0$ and thus $\psi_j$ experience exponential growth. Using the above arguments, we find the following for the BD and DB solitons in bands I and IV and bands II and III (as well as I and III).

*a. BD solitons in bands I and IV.* In this case $s = 1$, $d < 0$, and $V_{1(0)} = 0$; hence $\rho_1\rho_2 < 0$ and the cw background of the dark soliton component is modulationally unstable.

*b. DB solitons in bands II and III.* In this case $s = -1$, $d > 0$, and $V_{2(0)} = 0$; hence $\rho_1\rho_2 < 0$ and the cw background of the dark soliton component is modulationally unstable.

*c. DB solitons in bands I and III.* In this case $s = 1$, $d > 0$, and $V_{2(0)} = 0$. Contrary to the previous cases, we now have $\rho_1\rho_2 > 0$ and therefore the cw background of the dark soliton component is modulationally stable.

The above results qualitatively explain the different long-time behavior of the BD and DB solitons in bands I and IV and bands II and III [see snapshots at $t = 5 \times 10^5$ and at $t = 2 \times 10^5$ in Figs. 10(b) and 16(b), respectively] and DB solitons in bands I and III [see snapshot at $t = 5 \times 10^5$ in Fig. 14(b)].

[1] *Negative-Refraction Metamaterials: Fundamental Principles and Applications*, edited by G. V. Eleftheriades and K. G. Balmain (Wiley, Hoboken, 2005).

[2] C. Caloz and T. Itoh, *Electromagnetic Metamaterials: Transmission Line Theory and Microwave Applications* (Wiley, Hoboken, 2006).

[3] R. Marqués, F. Martín, and M. Sorolla, *Metamaterials with Negative Parameters: Theory, Design, and Microwave Applications* (Wiley, Hoboken, 2008).

[4] A. Lai, C. Caloz, and T. Itoh, IEEE Microwave Mag. **5**, 34 (2004).

[5] M. Lapine, M. Gorkunov, and K. H. Ringhofer, Phys. Rev. E **67**, 065601 (2003); M. Lapine and M. Gorkunov, *ibid.* **70**, 066601 (2004); B. Wang, J. Zhou, T. Koschny, and C. M. Soukoulis, Opt. Express **16**, 16058 (2008); D. A. Powell, I. V. Shadrivov, and Yu. S. Kivshar, Appl. Phys. Lett. **95**, 084102 (2009).

[6] J. Carbonell, V. E. Boria, and D. Lippens, Microwave Opt. Tech. Lett. **50**, 474 (2008).

[7] A. P. Slobozhanyuk, P. V. Kapitanova, I. V. Shadrivov, P. A. Belov, and Yu. S. Kivshar, JETP Lett. **95**, 613 (2012).

[8] S. Feng and K. Halterman, Phys. Rev. Lett. **100**, 063901 (2008).

[9] A. Chowdhury and J. A. Tataronis, Phys. Rev. Lett. **100**, 153905 (2008).

[10] A. B. Kozyrev and D. W. van der Weide, IEEE Trans. Microwave Theory Tech. **53**, 238 (2005).

[11] K. Narahara, T. Nakamichi, T. Suemitsu, T. Otsuji, and E. Sano, J. Appl. Phys. **102**, 024501 (2007).

[12] S. Gupta and C. Caloz, in *Proceedings of the IEEE MTT-S International Microwave Symposium, Honolulu, 2007* (IEEE, Piscataway, NJ, 2007), pp. 979–982; D. Yemélé and F. Kenmogné, Phys. Lett. A **373**, 3801 (2009).

[13] A. B. Kozyrev and D. W. van der Weide, J. Phys. D **41**, 173001 (2008).

[14] J. Ogasawara and K. Narahara, IEICE Electron. Express **7**, 608 (2010).

[15] L. Q. English, S. G. Wheeler, Y. Shen, G. P. Veldes, N. Whitaker, P. G. Kevrekidis, and D. J. Frantzeskakis, Phys. Lett. A **375**, 1242 (2011).

[16] Z. Wang, Y. Feng, B. Zhu, J. Zhao, and T. Jiang, J. Appl. Phys. **107**, 094907 (2010).

[17] Y. Inoue, J. Phys. Soc. Jpn. **43**, 243 (1977); T. Yoshinaga, N. Sugimoto, and T. Kakutani, *ibid.* **50**, 2122 (1981).

[18] J. M. Bilbault, P. Marquié, and B. Michaux, Phys. Rev. E **51**, 817 (1995); P. Marquié, J. M. Bilbault, and M. Remoissenet, *ibid.* **51**, 6127 (1995).

[19] M. Remoissenet, *Waves Called Solitons* (Springer, Berlin, 1999).

[20] Yu. S. Kivshar and G. P. Agrawal, *Optical Solitons: From Fibers to Photonic Crystals* (Academic, San Diego, 2003).

[21] M. J. Ablowitz, B. Prinari, and A. D. Trubatch, *Discrete and Continuous Nonlinear Schrödinger Systems* (Cambridge University Press, Cambridge, 2004).

[22] P. Marquie, J. M. Bilbault, and M. Remoissenet, Phys. Rev. E **49**, 828 (1994).

[23] G. P. Veldes, J. Cuevas, P. G. Kevrekidis, and D. J. Frantzeskakis, Phys. Rev. E **83**, 046608 (2011).

[24] G. P. Agrawal, Phys. Rev. Lett. **59**, 880 (1987).

[25] M. J. Ablowitz, S. D. Nixon, and Y. Zhu, Phys. Rev. A **79**, 053830 (2009); O. Bahat-Treidel, O. Peleg, M. Segev, and H. Buljan, *ibid.* **82**, 013830 (2010).

[26] L. H. Haddad and L. D. Carr, Physica D **238**, 1413 (2009); C. Becker, P. Soltan-Panahi, J. Kronjäger, S. Dörscher, K. Bongs, and K. Sengstock, New J. Phys. **12**, 065025 (2010).

[27] M. I. Molina and Yu. S. Kivshar, Opt. Lett. **35**, 2895 (2010); M. J. Ablowitz and Y. Zhu, *ibid.* **36**, 3762 (2011).

[28] C. L. Fefferman and M. I. Weinstein, J. Amer. Math. Soc. **25**, 1169 (2012); see also arXiv:1212.6072.

[29] *Emergent Nonlinear Phenomena in Bose-Einstein Condensates*, edited by P. G. Kevrekidis, D. J. Frantzeskakis, and R. Carretero-González (Springer-Verlag, Heidelberg, 2008); R. Carretero-González, D. J. Frantzeskakis, and P. G. Kevrekidis, Nonlinearity **21**, R139 (2008).

[30] J. Yang, Physica D **108**, 92 (1997).

[31] S. V. Manakov, Zh. Eksp. Teor. Fiz. **65**, 505 (1973) [Sov. Phys. JETP **38**, 248 (1973)].

[32] A. Jeffrey and T. Kawahara, *Asymptotic Methods in Nonlinear Wave Theory* (Pitman, Boston, 1982).